

Exploiting Completeness Perception with Diffusion Transformer for Unified 3D MRI Synthesis

Junkai Liu¹, Nay Aung^{2,3}, Theodoros N. Arvanitis¹, Joao A. C. Lima⁴,
Steffen E. Petersen^{2,3}, Daniel C. Alexander⁵, Le Zhang^{1,2}

¹School of Engineering, University of Birmingham, UK

²William Harvey Research Institute, Queen Mary University London, UK

³Barts Heart Centre, St Bartholomew’s Hospital, Barts Health NHS Trust, UK

⁴Division of Cardiology, Johns Hopkins University School of Medicine, US

⁵Department of Computer Science, University College London, UK

jx11920@student.bham.ac.uk; l.zhang.16@bham.ac.uk

Abstract

*Missing data problems, such as missing modalities in multi-modal brain MRI and missing slices in cardiac MRI, pose significant challenges in clinical practice. Existing methods rely on external guidance to supply detailed missing state for instructing generative models to synthesize missing MRIs. However, manual indicators are not always available or reliable in real-world scenarios due to the unpredictable nature of clinical environments. Moreover, these explicit masks are not informative enough to provide guidance for improving semantic consistency. In this work, we argue that generative models should infer and recognize missing states in a self-perceptive manner, enabling them to better capture subtle anatomical and pathological variations. Towards this goal, we propose CoPeDiT, a general-purpose latent diffusion model equipped with **completeness perception** for unified synthesis of 3D MRIs. Specifically, we incorporate dedicated pretext tasks into our tokenizer, CoPeVAE, empowering it to learn completeness-aware discriminative prompts, and design MDiT3D, a specialized diffusion transformer architecture for 3D MRI synthesis, that effectively uses the learned prompts as guidance to enhance semantic consistency in 3D space. Comprehensive evaluations on three large-scale MRI datasets demonstrate that CoPeDiT significantly outperforms state-of-the-art methods, achieving superior robustness, generalizability, and flexibility. The code is available at <https://github.com/JK-Liu7/CoPeDiT>.*

1. Introduction

Magnetic resonance imaging (MRI) is widely used in clinical medicine due to its non-invasive nature and ability to visualize detailed tissue properties [8]. For instance, multi-modal brain MRIs provide complementary information regarding brain anatomy and pathology [27], while volumetric cardiac MRIs reveal detailed cardiac structure and tissue characteristics [7]. However, brain and cardiac MRIs often suffer from missing data in real-world clinical settings [50]. For brain MRIs, certain modalities may be unavailable, while for cardiac MRIs, some slices may be missing, which are commonly caused by limited scanning time, image corruption, and variations in acquisition protocols [33].

To address this, generative models have been developed to infer missing data from observed inputs [11, 19]. Existing paradigms rely on auxiliary embeddings, e.g., binary mask codes, as prior knowledge to encode missing patterns (e.g., severity, type, and position) [6, 14, 21, 24, 29]. Nonetheless, this approach has several inherent limitations that hinder its practical applicability. First, in real-world deployments, input images may originate from different hospitals, scanners, or time points. As missing patterns are intrinsically unpredictable, providing manually defined masks in advance is impractical [41, 48]. Second, this over-reliance on predefined masks causes generative models to be unaware of the missing state and unable to distinguish between different modalities or spatial characteristics, thereby reducing robustness to variable and unseen incomplete patterns [20, 22, 51]. Models conditioned on fixed mask representations often suffer from limited generalizability, exhibiting noticeable drop in synthesis quality when encountering unfamiliar missing sites [2, 13, 32]. Fi-

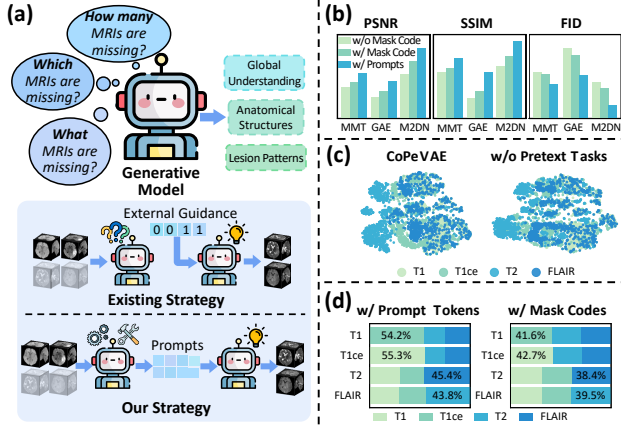


Figure 1. The motivation of CoPeDiT. (a) Comparison of completeness perception between CoPeDiT and prior methods. (b) Prompt tokens offer more effective guidance than binary mask codes. (c) CoPeVAE enables more discriminative latent representations. (d) Prompt tokens yield more semantically consistent attention maps in MDiT3D blocks, highlighting stronger interactions between similar modalities (e.g., T1-T1ce, T2-FLAIR).

nally, binary mask codes lack semantic richness and adaptability, leading to a rigid guidance that weakens spatial alignment and semantic coherence in the synthesized output [17, 37, 44].

Intuitively, generative models should be capable of inferring and detecting the incomplete state spontaneously, rather than relying on externally manual guidance [12, 17]. Motivated by this, we pose a central question: ‘*Can we empower the model with the ability to perceive missing states on its own?*’ In light of this, we exploit a long neglected and underexplored property of generative models in medical imaging, i.e., ‘*completeness perception*’, to enhance flexibility and generalizability under arbitrary missing MRI conditions, as illustrated in Fig. 1 (a). Our fundamental insight is to enable the generative model to recognize the fine-grained incomplete state information in a self-perceptive manner, and to leverage this understanding as internal prompts to guide the generation process. We hypothesize that, for diffusion models, such self-guided prompts may serve as an effective alternative to manually defined masks, and potentially offer even stronger guidance signals (Fig. 1 (b)). The main reason lies in the fact that this self-perceptive strategy encourages the model to learn both global and local anatomical structures and lesion patterns at coarse and fine levels, thus enabling more semantically coherent generation of the missing MRI regions during synthesis (Fig. 1 (c)(d)) [18, 23].

Driven by our motivation, we propose CoPeDiT, a 3D latent diffusion model (LDM) framework for unified 3D MRI synthesis. Technically, our framework builds on two core components: (i) Unlike prior approaches that require

explicit missing indicators, a novel tokenizer with a completeness perception function, CoPeVAE, is proposed to autonomously assess the integrity of modalities or volumes through tailored self-supervised pretext tasks. By detecting anatomical structures and variations in lesion patterns, CoPeVAE develops a comprehensive understanding of 3D MRIs. This enables CoPeDiT to eliminate the need for manual intervention with flexible adaptability, enhancing the method’s autonomy and improves its feasibility for real-world clinical deployment with diverse missing patterns. (ii) A novel diffusion transformer architecture, MDiT3D, is developed to unlock the potential of Diffusion Transformers (DiT) [34] for medical image synthesis, offering a new paradigm for generating high-quality volumetric data. MDiT3D leverages tokenization and attention mechanisms to model long-range and irregular contextual dependencies in high-dimensional, structurally complex 3D MRIs. It supports conditional generation guided by completeness-aware prompts, which provide semantic-meaningful guidance on the synthesis process. The learned prompt tokens comprehensively absorb information from available modalities or slices during the diffusion process and guide the generation of the missing ones. Incorporating the above two innovations, our architecture not only enables adaptive self-guidance synthesis in a mask-free manner which exhibits strong robustness and generalizability, but also demonstrates improved structural coherence and enhanced preservation of fine-grained anatomical details.

Our main contributions are summarized as follows:

- We propose a unified framework, dubbed CoPeDiT, for both 3D brain and cardiac missing MRI synthesis under arbitrary incomplete scenarios, without the need for explicit external indicators as guidance.
- We empower our tokenizer, CoPeVAE, with a strong capacity to perceive completeness by seamlessly integrating carefully designed pretext tasks, enabling the model to recognize missing states and learn informative, self-guided prompts.
- We present MDiT3D, a novel latent diffusion transformer for 3D MRI synthesis, featuring a dedicated architecture for capturing modality/spatial relationships and leveraging generated prompts as conditional guidance.
- Extensive experiments on three datasets demonstrate that our model surpasses state-of-the-art (SOTA) methods, achieving generalizability, robustness, and real-world clinical applicability.

2. Related Work

MRI Synthesis. Recent efforts focus on unified MRI synthesis using generative models such as Generative Adversarial Networks (GAN) and diffusion models [1, 36, 52, 56]. For example, MMGAN [43] employs a single network to handle diverse missing configurations, while Hyper-

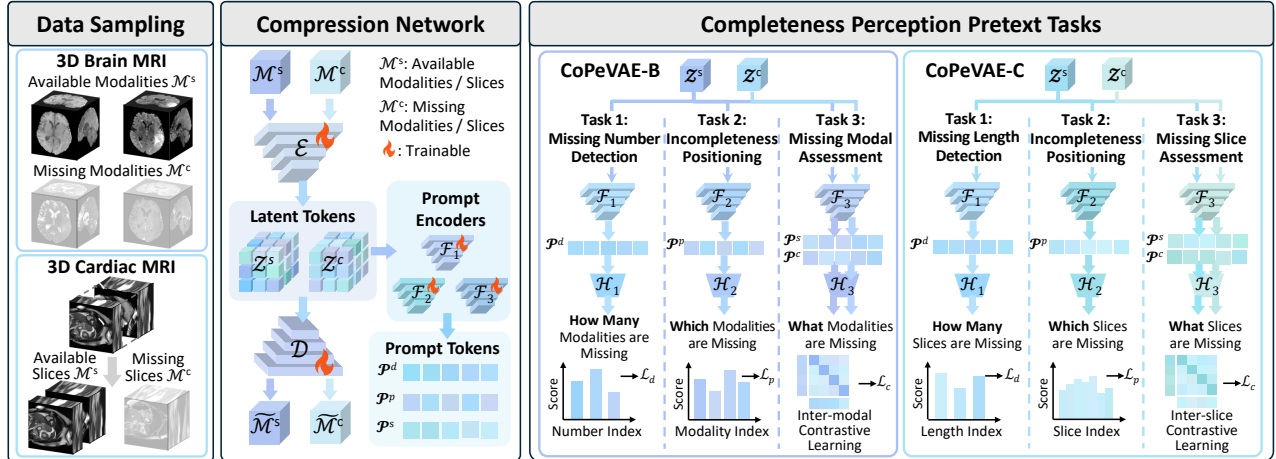


Figure 2. The overview framework of CoPeVAE. We implement two variants, CoPeVAE-B and CoPeVAE-C, with slight architectural modifications for brain and cardiac MRI synthesis tasks, respectively.

GAE [53] introduces a shared hyper-encoder and decoder architecture with a graph-based fusion module for reconstructing missing brain MRIs. MMT [24] proposes to leverage Swin Transformers [25] to capture inter-modal dependencies. M2DN [29] presents a diffusion-based method that jointly models all modalities using a multi-input multi-output framework. Despite these advances, most existing methods still rely on externally provided masks to encode missing patterns in randomly incomplete cases. In contrast, CoPeDiT explores self-perceptive capability of generative models to autonomously recognize data completeness, enabling more flexible and high-fidelity MRI synthesis.

Diffusion Models. Diffusion models have shown strong generative capacities across various computer vision tasks [26, 28, 55]. Denoising Diffusion Probabilistic Models [16] generate images by gradually adding Gaussian noise and learning to reverse the process. LDM [39] improve efficiency by operating in a compressed latent space using autoencoders. Recently, Diffusion transformers [34] have been effective alternatives to U-Net [40] in LDMs, achieving competitive performance in natural image generation. However, most prior medical image generation approaches still rely on U-Net-based architectures as the diffusion backbone, leaving the potential of transformer-based diffusion models underexplored in this domain [31, 49]. In this paper, we devise MDiT3D, by replacing the U-Net backbone with a diffusion transformer and incorporating task-specific architectural modifications, MDiT3D is capable of generalizing to 3D MRI data and capturing long-range dependencies of high-dimensional 3D MRIs.

3. Methodology

3.1. Notations

We consider two 3D MRI synthesis tasks: brain missing modality synthesis and cardiac missing slice synthesis. To unify the formulation, let $\mathcal{M} = \{\mathbf{x}^i\}_{i=1}^m$ denote a complete MRI sample, where m is the total number of modalities or slices. The available and missing subsets are denoted as $\mathcal{M}^S = \{\mathbf{x}^{s_i}\}_{i=1}^s$ and $\mathcal{M}^C = \{\mathbf{x}^{c_i}\}_{i=1}^c$, respectively, with $m = s + c$. **(1) Brain missing modality synthesis:** \mathcal{M} represents all brain MRIs with m modalities, and the task is to infer \mathcal{M}^C from \mathcal{M}^S . **(2) Cardiac missing slice synthesis:** \mathcal{M} corresponds to a volume with m slices, where missing slices \mathcal{M}^C are consecutive, non-overlapping with \mathcal{M}^S , and are to be reconstructed from the available ones. Notably, our experimental setup considers randomly generated incomplete cases from all the possible combinations as input, with a varying number and length of missing modalities or slices, aiming to mimic real-world clinical environments.

3.2. Stage I: Completeness Perception Tokenizer

The core idea of CoPeVAE (Fig. 2) is that detecting the completeness of high-resolution MRI data enforces the model to perceive both global anatomy and local lesion patterns, thereby producing high-quality prompts as diffusion guidance. Building upon VQGAN [10, 47], we deploy a 3D autoencoder jointly trained with self-supervised pretext tasks. Each task employs a prompt encoder, denoted as $\mathcal{F}_1, \mathcal{F}_2$ and \mathcal{F}_3 , to transform latent tokens (learned by the encoder \mathcal{E}) into low-dimensional prompt tokens. All prompt encoders contain 3D Conv layers followed by spatial average pooling. Afterwards, task-specific projection heads are applied for multi-granular classification and contrastive learning.

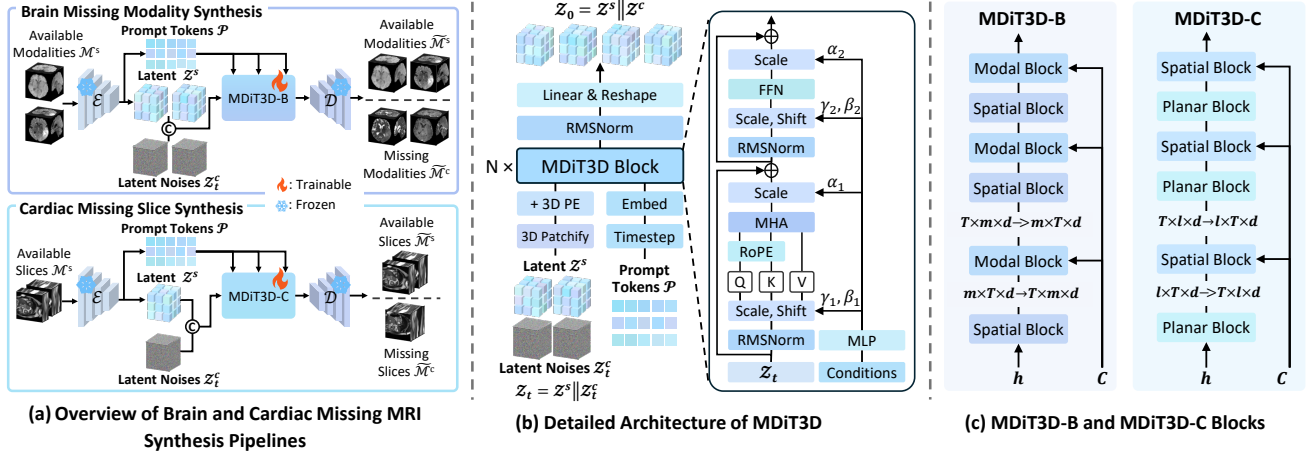


Figure 3. The overview framework of MDiT3D. PE and RoPE denote positional embeddings and rotary position embeddings [45, 54], respectively.

Data Sampling. To improve CoPeVAE’s adaptability to diverse missing cases, we employ a dual-random sampling strategy, where both the number/length of missing elements and the modality types/slice positions are randomly sampled. Given a complete set \mathcal{M} , we first randomly sample a missing count $c \in \{1, \dots, m-1\}$, then uniformly select c elements to form the missing subset \mathcal{M}^C , with the remainder forming the incomplete subset \mathcal{M}^S .

Task 1. Missing Number/Length Detection. Equipped with global contextual awareness, the tokenizer is capable of answering the question that how many modalities/slices are missing in the incomplete input. This task aims to enable the tokenizer to identify the severity of incompleteness by perceiving the global context of MRIs, thereby learning modality/spatial attributes in a coarse-grained manner. We formulate this task as an $(m-1)$ -class classification task and define the loss using the cross-entropy as

$$\mathcal{L}_d = \mathcal{L}_{\text{cls}}(\mathcal{H}_1(\mathcal{F}_1(\mathbf{z}^s)))_c. \quad (1)$$

where \mathcal{F}_1 and \mathcal{H}_1 represent the prompt encoder and the projection head for missing detection, respectively. The learned prompt tokens $\mathbf{p}^d = \mathcal{F}_1(\mathbf{z}^s)$ are rich in information about the severity of missing state.

Task 2. Incompleteness Positioning. By identifying which modalities or slices are missing, CoPeVAE yields prompt tokens $\mathbf{p}^p = \mathcal{F}_2(\mathbf{z}^s)$ that capture semantically meaningful local properties. The motivation of this task is to drive the model to develop a finer-grained contextual understanding of subtle anatomical structures and detailed pattern variations. Although the missing position implicitly encodes the count, Task 1 learns a modality/slice-agnostic global magnitude prior that calibrates the conditioning strength, while this task provides discrete, spatially localized cues about the exact missing identity. The incorporation of the two tasks improves robustness to errors from either signal. This task

is formulated as an m -class classification problem and is also optimized using the cross-entropy loss, defined as follows:

$$\mathcal{L}_p = \mathcal{L}_{\text{cls}}(\mathcal{H}_2(\mathcal{F}_2(\mathbf{z}^s)))_I. \quad (2)$$

where I denotes the index of missing type/position.

Task 3. Missing Modality/Slice Assessment. Motivated by the observation that modalities or slices from the same scan share more similar anatomical and textural context than those from different scans, we adopt an inter-modal/inter-slice contrastive learning scheme [38] to serve as a missing data estimator. Specifically, we take the incomplete latent tokens \mathbf{z}^s as anchor, the corresponding missing latent \mathbf{z}^c from the same subject as positives, and latent tokens \mathbf{z}^c from different subjects as negatives. The contrastive loss is defined as follows:

$$\mathcal{L}_c = -\log \frac{\varphi(\mathcal{H}_3(\mathbf{p}^s), \mathcal{H}_3(\mathbf{p}^c))}{\varphi(\mathcal{H}_3(\mathbf{p}^s), \mathcal{H}_3(\mathbf{p}^c)) + \sum \varphi(\mathcal{H}_3(\mathbf{p}^s), \mathcal{H}_3(\mathbf{p}^-))}. \quad (3)$$

where $\mathbf{p}^s = \mathcal{F}_3(\mathbf{z}^s)$, $\mathbf{p}^c = \mathcal{F}_3(\mathbf{z}^c)$, $\varphi(a, b) = \exp(a \cdot b / \tau)$, and τ is the temperature parameter. This contrastive learning scheme encourages the model to focus on inter-modal/slice contextual differences, thus improving anatomical coherence and fine-grained detail preservation. The overall loss of CoPeVAE is formulated as

$$\mathcal{L}_{\text{tok}} = \mathcal{L}_{\text{rec}} + \lambda(\mathcal{L}_d + \mathcal{L}_p + \mathcal{L}_c). \quad (4)$$

where λ is the weighting coefficient, and \mathcal{L}_{rec} denotes the reconstruction loss that consists of a pixel-wise L1 loss, vector quantization loss, adversarial loss, and perceptual loss.

3.3. Stage II: 3D MRI Diffusion Transformer

We propose MDiT3D (see Fig. 3), extending the model configuration of DiT [34] with several key design innovations to enable MDiT3D to adapt to 3D modalities and

Table 1. Quantitative results for multi-modal **brain MRI synthesis** on BraTS and IXI datasets. The numbers of the second row denote the number of missing modalities. The best performances are **bolded**.

	BraTS									IXI					
	1			2			3			1			2		
	PSNR↑	SSIM↑	FID↓												
<i>GAN-based Methods</i>															
MMGAN [43]	24.71 ±1.57	0.817 ±0.027	27.94 ±1.05	24.38 ±1.74	0.806 ±0.023	32.48 ±1.66	24.06 ±1.92	0.794 ±0.031	39.37 ±2.10	22.29 ±1.35	0.684 ±0.015	70.91 ±3.64	21.13 ±1.49	0.668 ±0.019	93.57 ±3.42
MMT [24]	25.19 ±1.41	0.824 ±0.017	24.53 ±1.33	24.50 ±1.55	0.811 ±0.020	29.57 ±1.82	23.92 ±1.53	0.801 ±0.021	39.66 ±1.95	22.64 ±1.49	0.698 ±0.013	53.60 ±3.14	21.82 ±1.60	0.687 ±0.019	72.24 ±2.98
Hyper-GAE [53]	24.65 ±1.62	0.813 ±0.022	28.97 ±1.57	24.42 ±1.74	0.808 ±0.024	33.52 ±1.78	23.86 ±1.88	0.788 ±0.029	41.79 ±2.21	22.12 ±1.33	0.682 ±0.017	72.62 ±3.78	20.91 ±1.45	0.662 ±0.021	98.79 ±4.05
<i>Diffusion Model-based Methods</i>															
LDM [39]	23.84 ±1.52	0.805 ±0.019	36.47 ±1.54	23.12 ±1.64	0.798 ±0.021	45.93 ±2.41	22.65 ±1.77	0.791 ±0.025	52.50 ±2.07	21.36 ±1.28	0.679 ±0.016	86.62 ±3.86	20.94 ±1.53	0.654 ±0.020	112.57 ±5.02
ControlNet [58]	23.98 ±1.49	0.808 ±0.018	34.09 ±1.93	23.34 ±1.60	0.801 ±0.020	41.28 ±2.49	22.85 ±1.68	0.795 ±0.022	48.07 ±1.99	21.83 ±1.51	0.681 ±0.015	81.26 ±3.85	21.07 ±1.50	0.661 ±0.019	103.77 ±5.17
M2DN [29]	26.45 ±1.36	0.830 ±0.016	21.29 ±1.18	25.87 ±1.48	0.820 ±0.017	27.36 ±1.62	25.21 ±1.59	0.809 ±0.024	32.40 ±1.93	23.47 ±1.43	0.715 ±0.014	42.52 ±3.08	22.81 ±1.56	0.702 ±0.018	55.64 ±3.62
CoPeDiT	28.26 ±1.24	0.842 ±0.019	12.67 ±0.98	28.13 ±1.49	0.831 ±0.021	13.25 ±1.45	27.91 ±1.41	0.822 ±0.023	14.89 ±1.61	24.34 ±1.21	0.732 ±0.016	25.84 ±2.58	23.92 ±1.53	0.721 ±0.020	32.53 ±3.16

volumetric MRI. It takes the high-dimensional latent tokens \mathbf{z}^s as input, along with the learned prompt tokens $\mathbf{p} = \mathbf{p}^d \parallel \mathbf{p}^p \parallel \mathbf{p}^s$ from our CoPeVAE tokenizer, which encode comprehensive missing state information and serve as conditional guidance for synthesizing. Without loss of generality, we use MDiT3D-B as a representative configuration to illustrate the architectural design.

3D Patchify & 3D Positional Embeddings. We apply a 3D patchify operator with patch size $p \times p \times p$ to obtain $\mathbf{h} \in \mathbb{R}^{m \times T \times d}$ [30], where m denotes the number of modalities, and d is the embedding dimension. Unlike the standard 2D positional embeddings [9] used in DiT, we leverage 3D frequency-based sine-cosine positional embeddings (3D PE) to better encode spatial positional information within the 3D MRI data.

Alternating Blocks & Prompt Injection. Two distinct types of blocks are designed tailored for brain and cardiac tasks, respectively. For the brain MRI synthesis task, we adopt spatial and modal blocks: the former focuses on capturing 3D spatial information, while the latter models inter-modal relationships. Before each modal block, the tokens \mathbf{h} are reshaped into $\mathbb{R}^{T \times m \times d}$ to facilitate inter-modal interaction, then reshaped back for subsequent spatial processing. These two types of blocks are stacked in an alternating fashion to form a total of N blocks. The motivation behind this design lies in the need for the model to capture both inter- and intra-modal relationships to boost contextual understanding and anatomical consistency. Additionally, adaptive layer normalization is employed to inject prompts into the blocks. Notably, inspired by the intuition that conditioning signals should be subtle yet informative, prompt tokens are injected only into the modal blocks.

Joint Reconstruction & Synthesis. We concatenate the available and the noisy latent (corresponding to missing sections) as the input to MDiT3D. Moreover, a joint reconstruction & synthesis scheme is introduced, where only the missing sections undergo noise injection and denoising during the diffusion process, while the observed regions remain unchanged, serving as auxiliary context that provides rich semantic guidance for generation. Given that directly synthesizing the entire modality/volume is more informa-

tive and efficient than simply predicting zero noise for the available latent regions [29], we adopt x-prediction loss as objective function for MDiT3D, as below:

$$\mathcal{L}_{\text{diff}} = \mathbb{E}_{\mathbf{z}_0, \epsilon, t} [\|\mathbf{z}_0 - f_{\theta}(\mathbf{z}_t, t, \mathbf{p})\|_2^2]. \quad (5)$$

where $\mathbf{z}_0 = \mathbf{z}^s \parallel \mathbf{z}^c$ denotes the concatenated clean latent tokens, $\mathbf{z}_t = \mathbf{z}^s \parallel \mathbf{z}_t^c$ is the noisy input at timestep t , \mathbf{p} is the prompt tokens, and f_{θ} represents our MDiT3D model.

4. Experiments and Results

4.1. Experimental Setup

Datasets. (i) Brain MRI Datasets. We evaluate the effectiveness of CoPeDiT on two public brain MRI datasets: BraTS 2021 [3] and IXI [5]. The BraTS 2021 dataset includes 1251 subjects with multi-modal MRI scans across four modalities: T1, T1ce, T2, and FLAIR. The IXI dataset contains 577 subjects with three MRI modalities: T1, T2, and PD. **(ii) Cardiac MRI Datasets.** Missing slice synthesis experiments are conducted on four cardiac MRI datasets: UK Biobank (UKBB) [35], MESA [57], ACDC [4], and MSCMR [59]. The model is trained on the combined dataset including all four sources with 32,248 MRI volumes in total, while performance comparisons are conducted on the UKBB dataset. We randomly select 80% of the data for training and use the remaining 20% as the test set. Please refer to the supplementary material for more dataset details.

Implementation Details. The compression rate of CoPeVAE is set to (8, 8, 8). For hyperparameters, the dimension of each prompt token is set to 512, τ and λ are set to 0.2 and 1e-2, respectively. The model is trained with a global batch size of 8 for CoPeVAE-B and 64 for CoPeVAE-C, using a learning rate of 1e-4. Regarding MDiT3D, we set the number of time steps to 500 with linearly scaled noise scheduling. The model is trained for 100k steps with a global batch size of 32 and learning rate of 5e-5. All training is conducted on four NVIDIA A100 GPUs. More details are provided in the supplementary material.

4.2. Performance Comparison

Quantitative Results. We compare our method against six recent SOTA models for 3D brain and cardiac MRI synthe-

Table 2. Quantitative results for **Cardiac MRI synthesis** on UKBB dataset. The numbers of the second row denote the length of missing slices. The best performances are **bolded**.

	UKBB								
	8			16			24		
	PSNR \uparrow	SSIM \uparrow	FID \downarrow	PSNR \uparrow	SSIM \uparrow	FID \downarrow	PSNR \uparrow	SSIM \uparrow	FID \downarrow
	<i>GAN-based Methods</i>								
MMGAN [43]	25.81 \pm 0.86	0.815 \pm 0.012	16.68 \pm 0.93	24.35 \pm 0.84	0.793 \pm 0.009	27.52 \pm 0.90	23.06 \pm 1.08	0.776 \pm 0.018	45.88 \pm 1.32
MMT [24]	26.02 \pm 0.82	0.824 \pm 0.009	15.90 \pm 0.88	24.73 \pm 0.87	0.809 \pm 0.010	23.75 \pm 0.97	24.12 \pm 1.06	0.794 \pm 0.017	37.39 \pm 1.27
Hyper-GAE [53]	25.23 \pm 0.89	0.810 \pm 0.012	19.02 \pm 0.96	23.66 \pm 0.94	0.789 \pm 0.013	31.84 \pm 1.15	22.70 \pm 1.14	0.771 \pm 0.019	48.27 \pm 1.39
	<i>Diffusion Model-based Methods</i>								
LDM [39]	24.17 \pm 0.96	0.795 \pm 0.012	24.61 \pm 0.94	23.04 \pm 1.03	0.778 \pm 0.010	44.93 \pm 1.49	22.19 \pm 1.21	0.761 \pm 0.018	60.02 \pm 1.68
ControlNet [58]	24.62 \pm 0.91	0.801 \pm 0.012	22.47 \pm 1.06	23.30 \pm 0.98	0.784 \pm 0.014	37.51 \pm 1.55	22.46 \pm 1.16	0.765 \pm 0.020	54.93 \pm 1.74
M2DN [29]	25.48 \pm 0.79	0.814 \pm 0.011	17.72 \pm 0.85	24.62 \pm 0.87	0.803 \pm 0.011	24.15 \pm 1.06	24.03 \pm 0.99	0.780 \pm 0.021	40.08 \pm 1.59
CoPeDiT	26.42 \pm 0.81	0.831 \pm 0.013	15.53 \pm 0.88	26.07 \pm 0.74	0.826 \pm 0.013	18.21 \pm 0.90	25.39 \pm 0.86	0.817 \pm 0.016	25.84 \pm 1.22

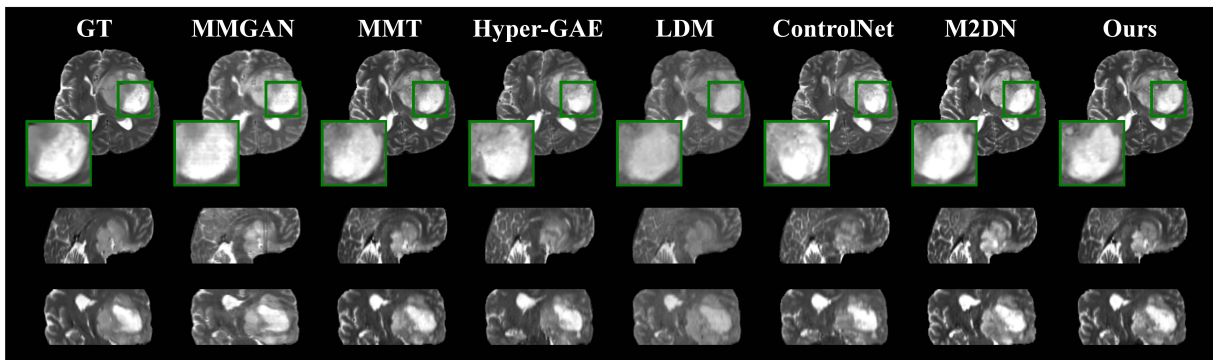


Figure 4. Qualitative results on BraTS dataset. The results are depicted in the axial (top), sagittal (middle) and coronal (bottom) views of the 3D MRI volume. The visual results on IXI dataset are provided in the supplementary material.

Table 3. Ablation study on the contribution of each pretext task to CoPeVAE’s reconstruction capacity. ‘Cardiac’ refers to the aggregated cardiac MRI dataset consisting of four sources, which are used for training our CoPeVAE model.

	BraTS		IXI		Cardiac	
	PSNR \uparrow	SSIM \uparrow	PSNR \uparrow	SSIM \uparrow	PSNR \uparrow	SSIM \uparrow
w/o Task 1	34.38	0.926	30.92	0.914	32.34	0.921
w/o Task 2	33.62	0.918	30.35	0.908	31.59	0.914
w/o Task 3	34.69	0.929	31.13	0.917	32.62	0.925
CoPeVAE	35.05	0.935	31.28	0.921	33.34	0.931

sis, including three GAN-based approaches [24, 43, 53] and three advanced diffusion model-based methods [29, 39, 58]. We report results by reimplementing all baselines from scratch under identical experimental settings to ensure fair comparisons. Performance is evaluated using three metrics: Peak Signal-to-Noise Ratio (PSNR), Structural Similarity Index Measure (SSIM), and Fréchet Inception Distance (FID) [15] that uses Inception-V3 [46] as the feature extractor. Quantitative results on the three datasets are presented in Tables 1 and 2, where the second row indicates the number of missing modalities or slices c , respectively. The results show that CoPeDiT consistently outperforms all baselines across all missing configurations in both synthesis tasks, showcasing superior generalizability. Notably, the

performance gains are more pronounced in scenarios with a larger number of missing modalities/slices, highlighting the robustness of our completeness-aware prompts in handling complex missing cases. Besides, CoPeDiT achieves significantly lower FID, indicating that the generated MRIs are more anatomically coherent and texture-preserving, with feature distributions that are closer to real clinical data, thus enhancing perceptual realism and diagnostic plausibility.

Qualitative Results. As depicted in Fig. 4 and 5, our model generates synthetic MRIs that exhibit the highest visual similarity to the ground truth images, particularly in accurately capturing tumor regions. Our CoPeDiT excels at preserving subtle textural details and modeling complex anatomical structures within brain tissues, justifying our motivation that incorporating completeness perception leads to improved anatomical consistency and realism.

4.3. Ablation Study

Effect of Pretext Tasks. As Table 3 displays, CoPeVAE preserves strong reconstruction capability while benefiting from the incorporation of pretext tasks. Each task contributes positively, and their combination leads to further improvements. This improvement can be attributed to the fact that pretext tasks promote the tokenizer to cap-

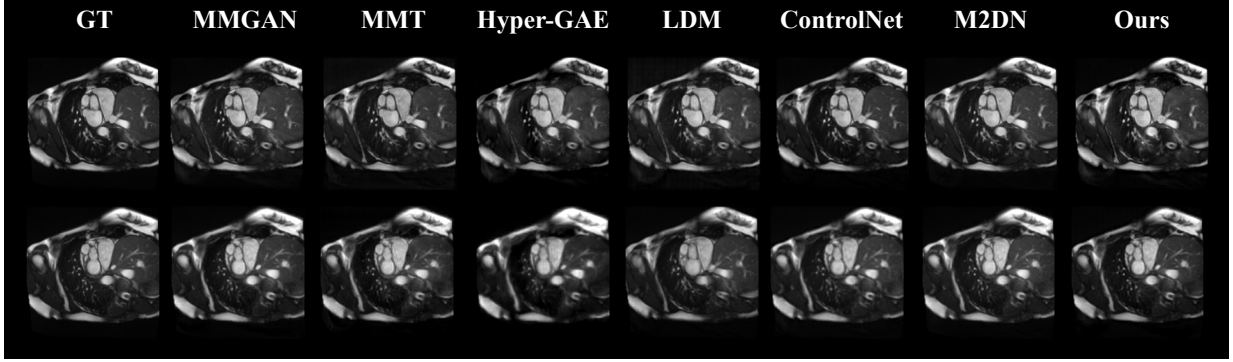


Figure 5. Qualitative results of comparison on UKBB dataset. The top and bottom results correspond to the first and last missing slices within a given volume, respectively.

Table 4. Ablation study on the contribution of completeness-aware prompt tokens.

	BraTS									UKBB					
	1			2			3			8			24		
	PSNR \uparrow	SSIM \uparrow	FID \downarrow	PSNR \uparrow	SSIM \uparrow	FID \downarrow	PSNR \uparrow	SSIM \uparrow	FID \downarrow	PSNR \uparrow	SSIM \uparrow	FID \downarrow	PSNR \uparrow	SSIM \uparrow	FID \downarrow
w/o \mathbf{p}^d	27.35	0.833	16.04	27.02	0.824	17.30	26.73	0.814	19.62	25.82	0.819	16.34	24.53	0.803	33.80
w/o \mathbf{p}^p	26.92	0.829	18.46	26.43	0.819	20.23	26.06	0.810	25.13	25.17	0.812	20.08	24.39	0.798	36.54
w/o \mathbf{p}^s	27.56	0.835	15.26	27.22	0.827	16.37	26.90	0.815	17.58	26.27	0.828	16.79	25.08	0.813	29.83
w/o Prompts	25.92	0.823	25.69	25.06	0.807	32.17	24.83	0.802	37.97	24.70	0.797	23.29	23.56	0.778	42.17
w/ Mask Codes	27.18	0.831	17.42	26.82	0.816	20.06	26.18	0.809	24.59	26.15	0.823	18.15	24.65	0.802	35.86
CoPeDiT	28.26	0.842	12.67	28.13	0.831	13.25	27.91	0.822	14.89	26.42	0.831	15.53	25.39	0.817	25.84

Table 5. Quantitative results by incorporating our learned prompt tokens into baselines instead of mask codes.

	BraTS		
	PSNR \uparrow	SSIM \uparrow	FID \downarrow
MMT [24]	25.19	0.824	24.53
+ Prompts (ours)	25.68 (+0.49)	0.826 (+0.002)	22.07 (-2.46)
Hyper-GAE [53]	24.65	0.813	28.97
+ Prompts (ours)	25.26 (+0.61)	0.822 (+0.009)	24.26 (-4.71)
M2DN [29]	26.45	0.830	21.29
+ Prompts (ours)	27.23 (+0.78)	0.837 (+0.007)	17.06 (-4.23)

ture anatomical structure variances in both coarse and fine-grained manner, learning highly discriminative features.

Effect of Prompt Tokens. Table 4 presents the synthesis performance associated with each learned prompt token and mask code. The mask codes are generated as one-hot vectors whose dimension corresponds to the number of modalities or slices, indicating the corresponding missing positions. Notably, we employ an identical injection strategy for all prompts and masks to ensure a fair comparison. As shown, all individual prompt tokens and their combinations improve model performance, surpassing guidance based on binary mask codes. These findings strongly highlight the effectiveness and rationale of our completeness perception scheme. The incompleteness positioning task yields the most effective prompts, likely due to its explicit emphasis on positioning missing sections along the modality/slice dimension, thus increasing the sensitivity to subtle structural variations. To further explore the potential of

our learned prompts, we incorporate them into prior baselines as replacements for mask codes. As illustrated in Table 13, this substitution consistently improves their performance, demonstrating the utility and generalizability of our completeness-aware prompts, which can serve as a flexible paradigm for improving emerging MRI synthesis methods.

Choice of Prompt Injection Position. This experiment aims to justify our choice of injecting prompts exclusively into the modal and spatial blocks for brain and cardiac tasks, respectively. As illustrated in Table 14, injecting prompts into the modal/spatial block yields the best overall performance, whereas injecting into spatial/planar blocks or both blocks results in inferior outcomes. This can be attributed to the fact that aligning the prompt with the block that explicitly models the task’s primary dependency, namely modality fusion for brain and through-plane continuity for cardiac, maximizes the efficacy of conditional signals.

Impact of 3D MRI Diffusion Transformer. The quantitative evaluation of MDiT3D and existing diffusion networks [30, 34, 39] is presented in Table 7. The results illustrate that MDiT3D consistently achieves superior performance, confirming that the specialized architectural designs effectively enhance the quality of 3D MRI synthesis.

4.4. Visualization Analysis

Salient Regions. To better understand the learning procedure of pretext tasks, we visualize their activation maps using GradCAM [42]. As shown in Fig. 6, the four examples reveal strong correlations between salient regions and

Table 6. Ablation study on the choice of prompt injection positions within the MDiT3D blocks. ‘Spatial / Planar’ indicates that prompt tokens are injected into the spatial and planar blocks for brain and cardiac tasks, respectively. ‘Both’ indicates that prompt tokens are injected into both the spatial and modal blocks for brain tasks, and into both the planar and spatial blocks for cardiac tasks. ‘Modal / Spatial’ indicates that prompt tokens are injected into the modal and spatial blocks, respectively.

	BraTS									UKBB					
	1			2			3			8			24		
	PSNR↑	SSIM↑	FID↓												
Spatial / Planar	27.47	0.834	15.41	27.20	0.825	16.83	27.03	0.817	17.45	26.29	0.827	16.82	25.22	0.814	29.24
Both	27.76	0.836	13.94	27.54	0.827	15.48	27.29	0.818	16.77	26.33	0.827	16.39	25.28	0.815	28.45
Modal / Spatial	28.26	0.842	12.67	28.13	0.831	13.25	27.91	0.822	14.89	26.42	0.831	15.53	25.39	0.817	25.84

Table 7. Ablation study on the contribution of 3D MRI Diffusion Transformer.

	BraTS									UKBB					
	1			2			3			8			24		
	PSNR↑	SSIM↑	FID↓												
UNet [39]	25.61	0.825	23.56	25.20	0.816	28.37	24.78	0.805	36.70	24.46	0.800	22.34	23.01	0.778	41.59
DiT [34]	26.78	0.835	19.72	26.14	0.823	21.84	25.74	0.808	24.47	25.89	0.825	16.28	24.78	0.799	36.10
DiT-3D [30]	26.84	0.835	19.23	26.23	0.822	21.95	25.90	0.810	26.08	26.08	0.825	16.37	24.83	0.806	33.73
MDiT3D	28.26	0.842	12.67	28.13	0.831	13.25	27.91	0.822	14.89	26.42	0.831	15.53	25.39	0.817	25.84

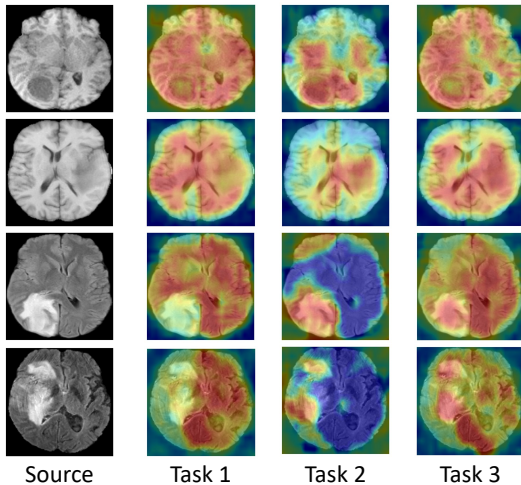


Figure 6. Visualization of salient regions on BraTS dataset.

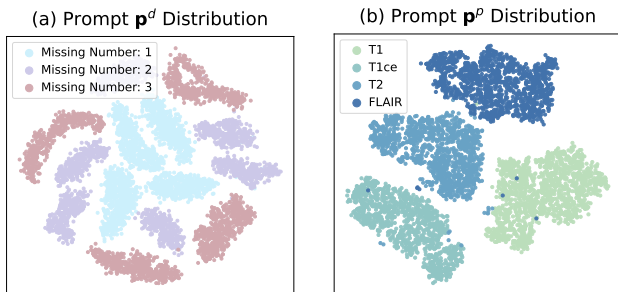


Figure 7. t-SNE visualization on the BraTS dataset of (a) The count-focused prompt \mathbf{p}^d colored by missing-number classes; and (b) The identity-focused prompt \mathbf{p}^p colored by missing modality.

modality-discriminative features. Specifically, these patterns mirror each task’s objective: Task 1 and Task 3 must

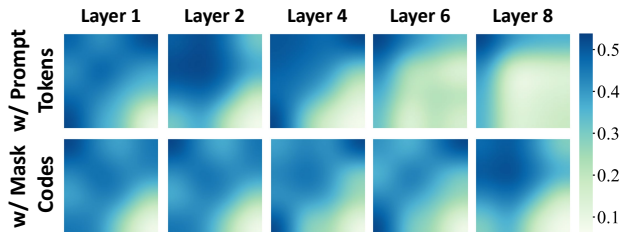


Figure 8. Visualization of attention maps from individual modal blocks on BraTS dataset under a missing configuration of [1, 0, 0, 0], where the first modality is absent.

assess global consistency, so they rely on coarse anatomical layout (gray and white matter) that summarize the volume. In contrast, Task 2 needs to pinpoint where/which is missing, so it keys on high-frequency, modality-specific cues (tumors, lesions, and white matter hyperintensities in FLAIR) to localize. The results emphasize that our pre-text tasks effectively capture modality-specific properties, understanding the MRI context and relationships.

Prompt Distribution. We implement the t-SNE visualization of learned prompts on BraTS and color them by ground-truth incompleteness labels. As depicted in Fig. 7, the count-focused prompt \mathbf{p}^d forms compact, well-separated clusters aligned with the missing number classes corresponding to each missing state (1/2/3 absent modalities), while the identity-focused prompt \mathbf{p}^p produces modality-specific clusters (T1, T1ce, T2, FLAIR) with clear boundaries, highlighting that the two prompts capture complementary aspects of incompleteness.

Attention Maps. We investigate the contribution of prompts by visualizing the attention maps of each modal block. As shown in Fig. 8, our prompts guide the attention

mechanism to progressively focus on the actual missing elements (the first row and column) with the increase of block layers. In comparison, mask codes lack sufficient informativeness and fail to provide nuanced guidance that aligns with the true missing state.

5. Conclusion

This work presents CoPeDiT, a unified model for 3D brain and cardiac MRI synthesis that explores completeness perception. We demonstrate that enabling the model to autonomously infer missing state, rather than relying on externally pre-defined masks, can provide more discriminative and informative guidance. To this end, we equip our tokenizer with completeness perception capability through elaborated pretext tasks. MDiT3D is then developed to utilize the learned prompt tokens as guidance for 3D MRI generation. Experimental evaluation validates the superiority of CoPeDiT in terms of accuracy, generalizability, robustness, and adaptability across diverse missing scenarios. Furthermore, CoPeDiT enables mask-free synthesis through perceiving completeness state, enhancing flexibility and applicability in practical clinical settings.

References

- [1] Suhyun Ahn, Wonjung Park, Jihoon Cho, and Jinah Park. Volumetric conditioning module to control pretrained diffusion models for 3d medical images. In *WACV*, pages 85–95, 2025. 2
- [2] Reza Azad, Mohammad Dehghanmanshadi, Nika Khosravi, Julien Cohen-Adad, and Dorit Merhof. Addressing missing modality challenges in mri images: A comprehensive review. *Computational Visual Media*, 11(2):241–268, 2025. 1
- [3] Ujjwal Baid, Satyam Ghodasara, Suyash Mohan, Michel Bilello, Evan Calabrese, Errol Colak, Keyvan Farahani, Jayashree Kalpathy-Cramer, Felipe C Kitamura, Sarthak Pati, et al. The rsna-asnr-miccai brats 2021 benchmark on brain tumor segmentation and radiogenomic classification. *arXiv preprint arXiv:2107.02314*, 2021. 5, 1
- [4] Olivier Bernard, Alain Lalonde, Clement Zotti, Frederick Cervenansky, Xin Yang, Pheng-Ann Heng, Irem Cetin, Karim Lekadir, Oscar Camara, Miguel Angel Gonzalez Ballester, Gerard Sanroma, Sandy Napel, Steffen Petersen, Georgios Tziritas, Elias Grinias, Mahendra Khened, Varghese Alex Kollerathu, Ganapathy Krishnamurthi, Marc-Michel Rohé, Xavier Pennec, Maxime Sermesant, Fabian Isensee, Paul Jäger, Klaus H. Maier-Hein, Peter M. Full, Ivo Wolf, Sandy Engelhardt, Christian F. Baumgartner, Lisa M. Koch, Jelmer M. Wolterink, Ivana Išgum, Yeonggul Jang, Yoonmi Hong, Jay Patravali, Shubham Jain, Olivier Humbert, and Pierre-Marc Jodoin. Deep learning techniques for automatic mri cardiac multi-structures segmentation and diagnosis: Is the problem solved? *IEEE Transactions on Medical Imaging*, 37(11):2514–2525, 2018. 5, 1
- [5] Imperial College London Brain Development Project. Ixi dataset (information extraction from images), 2025. Accessed 2025-07-28. 5, 1
- [6] Jihoon Cho, Jonghye Woo, and Jinah Park. A unified framework for synthesizing multisequence brain mri via hybrid fusion. *arXiv preprint arXiv:2406.14954*, 2024. 1
- [7] Sanuwani Dayarathna, Kh Tohidul Islam, Sergio Uribe, Guang Yang, Munawar Hayat, and Zhaolin Chen. Deep learning based synthesis of mri, ct and pet: Review and analysis. *Medical Image Analysis*, 92:103046, 2024. 1
- [8] Louise Dickinson, Hashim U Ahmed, Clare Allen, Jelle O Barentsz, Brendan Carey, Jurgen J Futterer, Stijn W Heijmink, Peter Hoskin, Alex P Kirkham, Anwar R Padhani, et al. Clinical applications of multiparametric mri within the prostate cancer diagnostic pathway. *Urologic oncology*, 31(3):281, 2013. 1
- [9] Alexey Dosovitskiy, Lucas Beyer, Alexander Kolesnikov, Dirk Weissenborn, Xiaohua Zhai, Thomas Unterthiner, Mostafa Dehghani, Matthias Minderer, Georg Heigold, Sylvain Gelly, et al. An image is worth 16x16 words: Transformers for image recognition at scale. *arXiv preprint arXiv:2010.11929*, 2020. 5
- [10] Patrick Esser, Robin Rombach, and Bjorn Ommer. Taming transformers for high-resolution image synthesis. In *CVPR*, pages 12873–12883, 2021. 3, 1
- [11] André Ferreira, Jianning Li, Kelsey L. Pomykala, Jens Kleesiek, Victor Alves, and Jan Egger. Gan-based generation of realistic 3d volumetric data: A systematic review and taxonomy. *Medical Image Analysis*, 93:103100, 2024. 1
- [12] Alexandros Graikos, Srikar Yellapragada, Minh-Quan Le, Saarthak Kapse, Prateek Prasanna, Joel Saltz, and Dimitris Samaras. Learned representation-guided diffusion models for large-image generation. In *CVPR*, pages 8532–8542, 2024. 2
- [13] Ibrahim Ethem Hamamci, Sezgin Er, Anjany Sekuboyina, Enis Simsar, Alperen Tezcan, Ayse Gulnihari Simsek, Sevval Nil Esirgun, Furkan Almas, Irem Doğan, Muhammed Furkan Dasdelen, et al. Generatect: Text-conditional generation of 3d chest ct volumes. In *ECCV*, pages 126–143, 2024. 1
- [14] Huaibo Hao, Jie Xue, Pu Huang, Liwen Ren, and Dengwang Li. Qgformer: Queries-guided transformer for flexible medical image synthesis with domain missing. *Expert Systems with Applications*, 247:123318, 2024. 1
- [15] Martin Heusel, Hubert Ramsauer, Thomas Unterthiner, Bernhard Nessler, and Sepp Hochreiter. Gans trained by a two time-scale update rule converge to a local nash equilibrium. In *NeurIPS*, 2017. 6
- [16] Jonathan Ho, Ajay Jain, and Pieter Abbeel. Denoising diffusion probabilistic models. In *NeurIPS*, pages 6840–6851, 2020. 3
- [17] Vincent Tao Hu, David W. Zhang, Yuki M. Asano, Gertjan J. Burghouts, and Cees G. M. Snoek. Self-guided diffusion models. In *CVPR*, pages 18413–18422, 2023. 2
- [18] Wuliang Huang, Yiqiang Chen, Xinlong Jiang, Chenlong Gao, Teng Zhang, Qian Chen, and Yifan Wang. Mitigating pervasive modality absence through multimodal generalization and refinement. In *AAAI*, pages 26796–26804, 2025. 2

- [19] Mahmoud Ibrahim, Yasmina Al Khalil, Sina Amirrajab, Chang Sun, Marcel Breeuwer, Josien Pluim, Bart Elen, Gökhan Ertaylan, and Michel Dumontier. Generative ai for synthetic data across multiple medical modalities: A systematic review of recent developments and challenges. *Computers in Biology and Medicine*, 189:109834, 2025. 1
- [20] Guanzhou Ke, Shengfeng He, Xiaoli Wang, Bo Wang, Guoqing Chao, Yuanyang Zhang, Yi Xie, and Hexing Su. Knowledge bridge: Towards training-free missing modality completion. In *CVPR*, pages 25864–25873, 2025. 1
- [21] Jonghun Kim and Hyunjin Park. Adaptive latent diffusion model for 3d medical image to image translation: Multimodal magnetic resonance imaging study. In *WACV*, pages 7604–7613, 2024. 1
- [22] Yi-Lun Lee, Yi-Hsuan Tsai, Wei-Chen Chiu, and Chen-Yu Lee. Multimodal prompting with missing modalities for visual recognition. In *CVPR*, pages 14943–14952, 2023. 1
- [23] Hanwen Liang, Niamul Quader, Zhixiang Chi, Lizhe Chen, Peng Dai, Juwei Lu, and Yang Wang. Self-supervised spatiotemporal representation learning by exploiting video continuity. In *AAAI*, pages 1564–1573, 2022. 2
- [24] Jiang Liu, Srivathsa Pasumarthi, Ben Duffy, Enhao Gong, Keshav Datta, and Greg Zaharchuk. One model to synthesize them all: Multi-contrast multi-scale transformer for missing data imputation. *IEEE Transactions on Medical Imaging*, 42(9):2577–2591, 2023. 1, 3, 5, 6, 7, 2
- [25] Ze Liu, Yutong Lin, Yue Cao, Han Hu, Yixuan Wei, Zheng Zhang, Stephen Lin, and Baining Guo. Swin transformer: Hierarchical vision transformer using shifted windows. In *ICCV*, pages 10012–10022, 2021. 3
- [26] Haoyu Lu, Guoxing Yang, Nanyi Fei, Yuqi Huo, Zhiwu Lu, Ping Luo, and Mingyu Ding. VDT: General-purpose video diffusion transformers via mask modeling. In *ICLR*, 2024. 3
- [27] Michael Lustig, David Donoho, and John M. Pauly. Sparse mri: The application of compressed sensing for rapid mr imaging. *Magnetic Resonance in Medicine*, 58(6):1182–1195, 2007. 1
- [28] Xin Ma, Yaohui Wang, Xinyuan Chen, Gengyun Jia, Ziwei Liu, Yuan-Fang Li, Cunjian Chen, and Yu Qiao. Latte: Latent diffusion transformer for video generation. *Transactions on Machine Learning Research*, 2025. 3
- [29] Xiangxi Meng, Kaicong Sun, Jun Xu, Xuming He, and Dinggang Shen. Multi-modal modality-masked diffusion network for brain mri synthesis with random modality missing. *IEEE Transactions on Medical Imaging*, 43(7):2587–2598, 2024. 1, 3, 5, 6, 7, 2
- [30] Shentong Mo, Enze Xie, Ruihang Chu, Lanqing Hong, Matthias Niessner, and Zhenguo Li. Dit-3d: Exploring plain diffusion transformers for 3d shape generation. In *NeurIPS*, pages 67960–67971, 2023. 5, 7, 8
- [31] Maham Nazir, Muhammad Aqeel, and Francesco Setti. Diffusion-based data augmentation for medical image segmentation. In *ICCV*, pages 1330–1339, 2025. 3
- [32] Tan Pan, Zhaorui Tan, Kaiyu Guo, Dongli Xu, Weidi Xu, Chen Jiang, Xin Guo, Yuan Qi, and Yuan Cheng. Structure-aware semantic discrepancy and consistency for 3d medical image self-supervised learning. In *ICCV*, pages 20257–20267, 2025. 1
- [33] Anthony Paproki, Olivier Salvado, and Clinton Fookes. Synthetic data for deep learning in computer vision & medical imaging: A means to reduce data bias. *ACM Computing Surveys*, 56(11), 2024. 1
- [34] William Peebles and Saining Xie. Scalable diffusion models with transformers. In *ICCV*, pages 4195–4205, 2023. 2, 3, 4, 7, 8
- [35] Steffen E. Petersen, Paul M. Matthews, Jane M. Francis, Matthew D. Robson, Filip Zemrak, Redha Boubertakh, Alistair A. Young, Sarah Hudson, Peter Weale, Steve Garratt, Rory Collins, Stefan Piechnik, and Stefan Neubauer. Uk biobank’s cardiovascular magnetic resonance protocol. *Journal of Cardiovascular Magnetic Resonance*, 18(1):8, 2016. 5, 1
- [36] Kunpeng Qiu, Zhiqiang Gao, Zhiying Zhou, Mingjie Sun, and Yongxin Guo. Noise-consistent siamese-diffusion for medical image synthesis and segmentation. In *CVPR*, pages 15672–15681, 2025. 2
- [37] Yansheng Qiu, Ziyuan Zhao, Hongdou Yao, Delin Chen, and Zheng Wang. Modal-aware visual prompting for incomplete multi-modal brain tumor segmentation. In *ACMMM*, page 3228–3239, 2023. 2
- [38] Alec Radford, Jong Wook Kim, Chris Hallacy, Aditya Ramesh, Gabriel Goh, Sandhini Agarwal, Girish Sastry, Amanda Askell, Pamela Mishkin, Jack Clark, Gretchen Krueger, and Ilya Sutskever. Learning transferable visual models from natural language supervision. In *ICML*, pages 8748–8763, 2021. 4
- [39] Robin Rombach, Andreas Blattmann, Dominik Lorenz, Patrick Esser, and Björn Ommer. High-resolution image synthesis with latent diffusion models. In *CVPR*, pages 10684–10695, 2022. 3, 5, 6, 7, 8, 2
- [40] Olaf Ronneberger, Philipp Fischer, and Thomas Brox. U-net: Convolutional networks for biomedical image segmentation. In *International Conference on Medical image computing and computer-assisted intervention*, pages 234–241. Springer, 2015. 3, 2
- [41] Shaohao Rui, Lingzhi Chen, Zhenyu Tang, Lilong Wang, Mianxin Liu, Shaoting Zhang, and Xiaosong Wang. Multi-modal vision pre-training for medical image analysis. In *CVPR*, pages 5164–5174, 2025. 1
- [42] Ramprasaath R. Selvaraju, Michael Cogswell, Abhishek Das, Ramakrishna Vedantam, Devi Parikh, and Dhruv Batra. Grad-cam: Visual explanations from deep networks via gradient-based localization. In *ICCV*, 2017. 7
- [43] Anmol Sharma and Ghassan Hamarneh. Missing mri pulse sequence synthesis using multi-modal generative adversarial network. *IEEE Transactions on Medical Imaging*, 39(4): 1170–1183, 2020. 2, 5, 6
- [44] Yejee Shin, Yeeun Lee, Hanbyol Jang, Geonhui Son, Hyeongyu Kim, and Dosik Hwang. Anatomical consistency and adaptive prior-informed transformation for multi-contrast mr image synthesis via diffusion model. In *CVPR*, pages 30918–30927, 2025. 2
- [45] Jianlin Su, Murtadha Ahmed, Yu Lu, Shengfeng Pan, Wen Bo, and Yunfeng Liu. Roformer: Enhanced transformer with rotary position embedding. *Neurocomputing*, 568:127063, 2024. 4

- [46] Christian Szegedy, Vincent Vanhoucke, Sergey Ioffe, Jon Shlens, and Zbigniew Wojna. Rethinking the inception architecture for computer vision. In *CVPR*, 2016. 6
- [47] Aaron van den Oord, Oriol Vinyals, and koray kavukcuoglu. Neural discrete representation learning. In *NeurIPS*, 2017. 3, 1
- [48] Hu Wang, Yuanhong Chen, Congbo Ma, Jodie Avery, Louise Hull, and Gustavo Carneiro. Multi-modal learning with missing modality via shared-specific feature modelling. In *CVPR*, pages 15878–15887, 2023. 1
- [49] Haoshen Wang, Zhentao Liu, Kaicong Sun, Xiaodong Wang, Dinggang Shen, and Zhiming Cui. 3d meddiffusion: A 3d medical latent diffusion model for controllable and high-quality medical image generation. *IEEE Transactions on Medical Imaging*, 2025. 3
- [50] Yulin Wang, Honglin Xiong, Kaicong Sun, Shuwei Bai, Ling Dai, Zhongxiang Ding, Jiameng Liu, Qian Wang, Qian Liu, and Dinggang Shen. Toward general text-guided multimodal brain mri synthesis for diagnosis and medical image analysis. *Cell Reports Medicine*, 2025. 1
- [51] Laura Wenderoth, Konstantin Hemker, Nikola Simidjievski, and Mateja Jamnik. Measuring cross-modal interactions in multimodal models. In *AAAI*, pages 21501–21509, 2025. 1
- [52] Yan Xia, Le Zhang, Nishant Ravikumar, Rahman Attar, Stefan K. Piechnik, Stefan Neubauer, Steffen E. Petersen, and Alejandro F. Frangi. Recovering from missing data in population imaging – cardiac mr image imputation via conditional generative adversarial nets. *Medical Image Analysis*, 67:101812, 2021. 2
- [53] Heran Yang, Jian Sun, and Zongben Xu. Learning unified hyper-network for multi-modal mr image synthesis and tumor segmentation with missing modalities. *IEEE Transactions on Medical Imaging*, 42(12):3678–3689, 2023. 3, 5, 6, 7, 2
- [54] Zhuoyi Yang, Jiayan Teng, Wendi Zheng, Ming Ding, Shiyu Huang, Jiazheng Xu, Yuanming Yang, Wenyi Hong, Xiaohan Zhang, Guanyu Feng, Da Yin, Yuxuan Zhang, Weihan Wang, Yean Cheng, Bin Xu, Xiaotao Gu, Yuxiao Dong, and Jie Tang. Cogvideox: Text-to-video diffusion models with an expert transformer. In *ICLR*, 2025. 4
- [55] Jingfeng Yao, Bin Yang, and Xinggang Wang. Reconstruction vs. generation: Taming optimization dilemma in latent diffusion models. In *CVPR*, pages 15703–15712, 2025. 3
- [56] Yousef Yeganeh, Azade Farshad, Ioannis Charisiadis, Marta Hasny, Martin Hartenberger, Björn Ommer, Nassir Navab, and Ehsan Adeli. Latent drifting in diffusion models for counterfactual medical image synthesis. In *CVPR*, pages 7685–7695, 2025. 2
- [57] Guo-Qiang Zhang, Licong Cui, Remo Mueller, Shiqiang Tao, Matthew Kim, Michael Rueschman, Sara Mariani, Daniel Mobley, and Susan Redline. The national sleep research resource: towards a sleep data commons. *Journal of the American Medical Informatics Association*, 25(10):1351–1358, 2018. 5, 1
- [58] Lvmin Zhang, Anyi Rao, and Maneesh Agrawala. Adding conditional control to text-to-image diffusion models. In *ICCV*, pages 3836–3847, 2023. 5, 6, 2
- [59] Xiahai Zhuang, Jiahang Xu, Xinzhe Luo, Chen Chen, Cheng Ouyang, Daniel Rueckert, Victor M. Campello, Karim Lekadir, Sulaiman Vesal, Nishant RaviKumar, Yashu Liu, Gongning Luo, Jingkun Chen, Hongwei Li, Buntheng Ly, Maxime Sermesant, Holger Roth, Wentao Zhu, Jiexiang Wang, Xinghao Ding, Xinyue Wang, Sen Yang, and Lei Li. Cardiac segmentation on late gadolinium enhancement mri: A benchmark study from multi-sequence cardiac mr segmentation challenge. *Medical Image Analysis*, 81:102528, 2022. 5, 1

Exploiting Completeness Perception with Diffusion Transformer for Unified 3D MRI Synthesis

Supplementary Material

A. Datasets

The details of the brain and cardiac MRI datasets used in our experiment are summarized in Table 8. Notably, we train our CoPeVAE and MDiT3D models on the brain MRI synthesis task on BraTS and IXI datasets separately, due to differences in the number and types of modalities. The evaluation and results are also reported for the two datasets separately. For Cardiac MRI synthesis, we leverage a combination of all four datasets to train both two-stage models.

Table 8. Details of brain and cardiac MRI datasets.

Datasets	Modality	Cases	Train	Test
<i>Brain MRI</i>				
BraTS [3]	T1, T1ce, T2, FLAIR	1251	1000	251
IXI [5]	T1, T2, PD	577	462	115
<i>Cardiac MRI</i>				
UKBB [35]	-	31350	25080	6270
MESA [57]	-	298	238	60
ACDC [4]	-	300	240	60
MSCMR [59]	-	300	240	60
Combined	-	32248	25798	6450

B. More Implementation Details

B.1. Data Preprocessing

Brain MRI data. Following [24, 29], we use 90 and 80 middle axial slices for BraTS and IXI datasets, respectively. These slices are further cropped to a size of 192×192 from the central region. Ultimately, all volumes are resized to a fixed size of $192 \times 192 \times 64$ to serve as model input.

Cardiac MRI data. All slices within each cardiac MRI volume are used and cropped to 192×192 from the central region. Each volume is then resized to a fixed size of $192 \times 192 \times 32$ for training and inference.

For all datasets, we apply intensity normalization by linearly scaling voxel intensities between the 0.5th and 99.5th percentiles to the range $[0, 1]$. The data augmentations we employ include random spatial cropping, rotation, flipping, scaling, and shifting.

B.2. Architecture of Prompt Encoders and Projection Heads

We devise three light weight prompt encoders to generate completeness-aware prompt tokens in our CoPeVAE, followed by three projection heads for each pretext task. The

Table 9. Detailed architecture of each prompt encoder and projection head in the pretext task.

Prompt Encoder	\mathcal{F}_1	\mathcal{F}_2	\mathcal{F}_3
Architecture	3D Conv (in 8, out 256)	3D Conv (in 8, out 256)	3D Conv (in 8, out 256)
	3D BatchNorm	3D BatchNorm	3D BatchNorm
	ReLU	ReLU	ReLU
	3D Conv (in 256, out 512)	3D Conv (in 256, out 512)	3D Conv (in 256, out 512)
	3D BatchNorm	3D BatchNorm	3D BatchNorm
	ReLU	ReLU	ReLU
	3D Adaptive Avg Pool	3D Adaptive Avg Pool	3D Adaptive Avg Pool
	Linear (512, 1024)	Linear (512, 1024)	Linear (512, 1024)
	ReLU	ReLU	ReLU
	Linear (1024, 512)	Linear (1024, 512)	Linear (1024, 512)
Projection Head	\mathcal{H}_1	\mathcal{H}_2	\mathcal{H}_3
Architecture	SiLU	SiLU	SiLU
	Linear (512, $m - 1$)	Linear (512, m)	Linear (512, 128)

detailed architecture of each prompt encoder and projection head is illustrated in Table 9.

Notably, in our framework, binary mask codes are only used in the pretraining of CoPeVAE, where we synthetically remove modalities/slices and supervise the pretext tasks with known missing patterns. Once CoPeVAE is trained, we freeze its parameters and use it as a completeness-aware tokenizer: given any incomplete MRI with an arbitrary missing pattern, CoPeVAE directly infers the corresponding completeness prompts $\mathbf{p} = \mathbf{p}^d \parallel \mathbf{p}^p \parallel \mathbf{p}^s$ from the observed data, without requiring explicit mask codes as input. During both diffusion model training and inference, the diffusion backbone receives only the latent representations and these learned prompts. The original binary masks that were used to generate synthetic missingness are not provided to the diffusion model. In this sense, our synthesis process is mask-free: CoPeDiT no longer depends on hand-crafted or externally supplied mask codes at the generation stage, but instead relies entirely on the learned completeness prompts produced by the frozen CoPeVAE.

B.3. Hyperparameter Setups

CoPeVAE. The detailed hyperparameter setup of CoPeVAE is provided in Table 10. Built upon VQVAE [47] and VQ-GAN [10], our model employs a codebook containing 8192 codes with the latent dimensionality of 8. The values of τ and λ are empirically set, as they have only a slight impact on model performance. The Adam optimizer is applied with a warmup cosine learning rate schedule. The training steps of CoPeVAE-B and CoPeVAE-C are 400k and 100k,

Table 10. Hyperparameter setup of CoPeVAE.

	CoPeVAE-B	CoPeVAE-C
Architecture		
Input dim.	$m \times 192 \times 192 \times 64$	$192 \times 192 \times 32$
Num. codebook	8192	8192
Latent dim.	8	8
Channels	(256, 384, 512)	(32, 64, 128)
Compression ratio	(8, 8, 8)	(8, 8, 8)
Prompt dim.	512	512
τ	0.2	0.2
λ	0.01	0.01
Optimization		
Batch size	8	64
Learning rate	1e-4	1e-4
Optimizer	Adam	Adam
(β_1, β_2)	(0.9, 0.999)	(0.9, 0.999)
LR schedule	Warmup cosine	Warmup cosine
Training steps	400k	200k

Table 11. Hyperparameter setup of MDiT3D.

	MDiT3D-B	MDiT3D-C
Architecture		
Input dim.	$m \times 8 \times 24 \times 24 \times 8$	$4 \times 8 \times 24 \times 24$
Hidden dim.	768	576
Num. blocks	16	12
Num. heads	12	12
Patch size	2	1
Params (M)	173.3	33.0
Flops (G)	555.1 (BraTS) 424.5 (IXI)	104.0
Optimization		
Batch size	32	64
Learning rate	5e-5	5e-5
Optimizer	AdamW	AdamW
(β_1, β_2)	(0.9, 0.999)	(0.9, 0.999)
LR schedule	Warmup cosine	Warmup cosine
Training steps	100k	100k
EMA decay	0.9999	0.9999
Interpolants		
Training objective	x-prediction	x-prediction
Noise schedule	scaled-linear	scaled-linear
Timesteps	500	500
Sampler	DDIM	DDIM
Sampling steps	200	250

respectively.

MDiT3D. For MDiT3D, we carefully design the hyperparameters to balance dataset size and model capacity, as summarized in Table 11. Following DiT [34], we report the experimental results using the exponential moving average (EMA) with a decay rate of 0.9999. During training, we set the timestep to 500 with linearly scaled noise levels ranging from 0.0015 to 0.0195. MDiT3D is trained for 100k

Table 12. Experimental results of tumor segmentation experiments on BraTS dataset.

	Dice Score (%) \uparrow			
	WT	TC	ET	AVG
Missing	86.08	84.67	81.59	84.11
<i>GAN-based Methods</i>				
MMGAN [43]	89.35	88.14	87.73	88.41
MMT [24]	90.43	88.37	86.92	88.57
Hyper-GAE [53]	88.72	86.54	85.37	86.88
<i>Diffusion Model-based Methods</i>				
LDM [39]	87.86	85.91	84.19	85.99
ControlNet [58]	88.27	87.05	85.23	86.85
M2DN [29]	91.28	90.09	88.20	89.86
CoPeDiT	91.35	90.41	88.94	90.23

iterations using the AdamW optimizer and a warmup cosine learning rate schedule. During inference, the DDIM sampler is applied with sample steps of 200 and 250 for MDiT3D-B and MDiT3D-C, respectively.

In addition, we use mixed-precision training with a gradient clipping to accelerate training and save computational resources throughout all two-stage experiments.

C. Additional Experimental Results

C.1. Qualitative Results

Fig. 9 provides the qualitative evaluation results of brain MRI synthesis on the IXI dataset. As shown, we can also observe that our CoPeDiT outperforms other baselines in preserving the intricate structures and texture information in the synthesized MRIs.

C.2. Tumor Segmentation

In this section, we evaluate the clinical utility of our synthesized MRIs through downstream tumor segmentation experiments on the BraTS dataset. Specifically, following [24, 29], we train a multi-modal U-Net [40] on the four MRI modalities, where one modality is withheld and replaced by the synthesized image generated by our CoPeDiT or competing baselines. Additionally, we implement a U-Net that takes only the three available modalities as input for comparison. We report the average Dice scores for whole tumor (WT), tumor core (TC), and enhancing tumor (ET), as summarized in Table 12. As shown, all methods improve the segmentation accuracy over the 'Missing' baseline that only uses the three available modalities, confirming the benefit of recovering the missing contrast. Among them, CoPeDiT achieves the best performance on all three tumor subregions, leading to the highest average Dice of 90.23%. These results demonstrate that our synthesized MRIs are not only

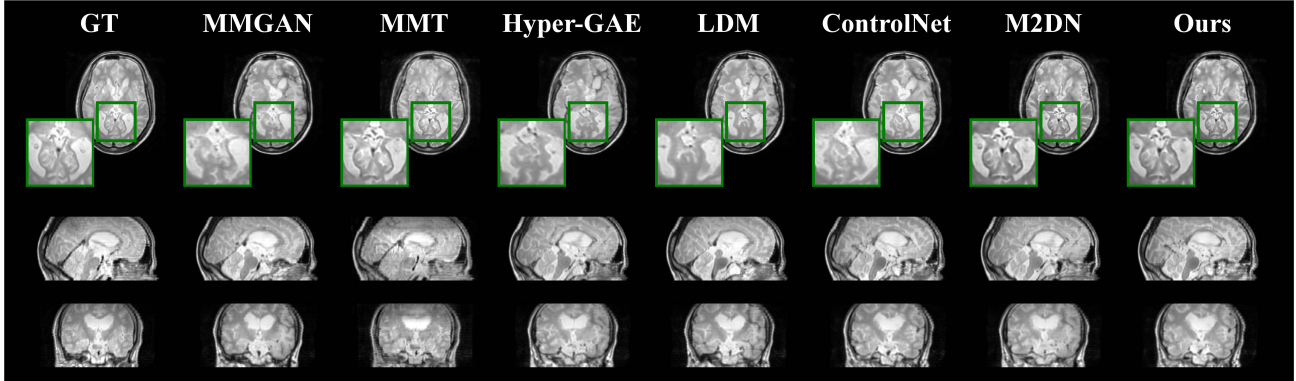


Figure 9. Qualitative results of comparison on IXI dataset. The results are depicted in the axial (top), sagittal (middle) and coronal (bottom) views of the 3D MRI volume.

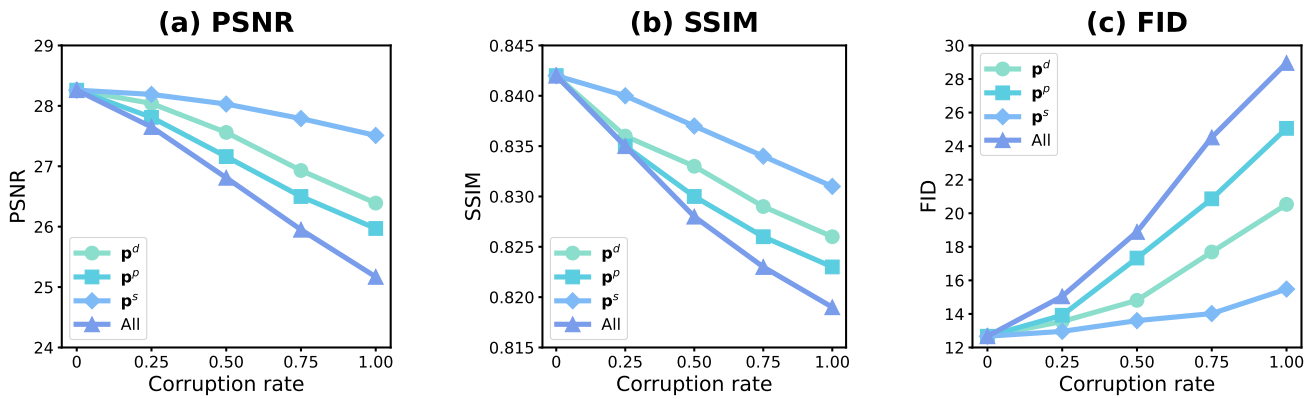


Figure 10. Sensitivity of CoPeDiT to prompt corruption on BraTS dataset.

Table 13. Ablation study on the contribution of completeness perception prompt tokens on the IXI dataset.

	IXI					
	1			2		
	PSNR \uparrow	SSIM \uparrow	FID \downarrow	PSNR \uparrow	SSIM \uparrow	FID \downarrow
w/o \mathbf{p}^d	23.56	0.720	35.93	23.04	0.708	48.71
w/o \mathbf{p}^p	22.81	0.697	50.70	21.99	0.692	63.16
w/o \mathbf{p}^s	24.17	0.724	31.89	23.56	0.710	39.87
w/o Prompts	22.48	0.696	57.64	21.67	0.683	81.49
w/ Mask Codes	23.35	0.711	44.03	22.84	0.702	56.72
CoPeDiT	24.34	0.732	25.84	23.92	0.721	32.53

visually plausible but also provide more informative inputs for downstream clinical tasks such as tumor segmentation.

C.3. Prompt Accuracy Sensitivity

To assess how sensitive CoPeDiT is to the correctness of completeness prompts, we conduct a controlled prompt corruption study on the BraTS dataset under the number of

Table 14. Quantitative results on the IXI dataset by incorporating our completeness perception prompt tokens into baseline methods instead of mask codes.

	IXI		
	PSNR \uparrow	SSIM \uparrow	FID \downarrow
MMT [24]	22.64	0.698	53.60
+ Prompts (ours)	23.19 (+0.55)	0.707 (+0.009)	46.13 (-7.47)
Hyper-GAE [53]	22.12	0.682	72.62
+ Prompts (ours)	22.46 (+0.34)	0.694 (+0.012)	59.43 (-13.19)
M2DN [29]	23.47	0.715	42.52
+ Prompts (ours)	23.84 (+0.37)	0.726 (+0.011)	33.79 (-8.73)

missing modalities of 1. Starting from a trained CoPeDiT and CoPeVAE, we consider the degree prompt \mathbf{p}^d (number/length of missing content), the position prompt \mathbf{p}^p (location of missing regions), and the semantic prompt \mathbf{p}^s . For each prompt type, we define a corruption rate $r \in \{0, 0.25, 0.5, 0.75, 1.0\}$. Given a rate r , we randomly

select an r -fraction of validation samples and replace the corresponding prompt with an incorrect one (sampled from other cases), while keeping all network weights and the other prompts unchanged. We also include an 'All' setting where all three prompts are corrupted simultaneously. As illustrated in Fig. 10, increasing the corruption rate consistently degrades synthesis quality in terms of all three metrics. This demonstrates that CoPeDiT relies on the accuracy of completeness prompts. Among the three types, corrupting the position prompt \mathbf{p}^p causes the largest synthesis performance drop, emphasizing that precise localization of missing regions is particularly critical. Corrupting the degree prompt \mathbf{p}^d also noticeably harms performance, whereas the semantic prompt \mathbf{p}^s is somewhat more robust but still shows a clear degradation trend. When all prompts are corrupted, performance deteriorates the most across all metrics, confirming that the three prompts provide complementary and influential guidance for high-fidelity synthesis.

C.4. Ablation Study

We further evaluate the effectiveness of our prompt token design on the IXI dataset. As shown in Table 13, the complete set of prompt tokens yields the best performance, outperforming both conventional mask codes and all individual prompt tokens. Furthermore, we apply our learned prompt tokens to other baseline models originally using mask codes. As illustrated in Table 14, our prompts also lead to consistent performance gains across all baselines. In summary, the effectiveness of our prompt learning scheme is validated on the IXI dataset through the additional evaluations presented above.